prosthesis

MDPI

Article

Optimizing Graded Porous Scaffolds for Bone Defects: Insights from In Vivo Mechanical Environments

Juan Mora-Macías [1,*], Jorge E. Santos [2], André P. G. Castro [2,3] and Paulo R. Fernandes [2]

[1] Departamento de Ingeniería Minera, Mecánica, Energética y de la Construcción, Escuela Técnica Superior de Ingeniería, Campus de «El Carmen», Universidad de Huelva, Avda. de las Fuerzas Armadas, s/n, 21007 Huelva, Spain
[2] IDMEC, Instituto Superior Técnico, Universidade de Lisboa, Av. Rovisco Pais, Nº 1, 1049-001 Lisboa, Portugal; jorge.e.santos@tecnico.ulisboa.pt (J.E.S.); andre.castro@tecnico.ulisboa.pt (A.P.G.C.); paulo.rui.fernandes@tecnico.ulisboa.pt (P.R.F.)
[3] ESTSetúbal, Instituto Politécnico de Setúbal, Campus do IPS–Estefanilha, 2914-508 Setúbal, Portugal
* Correspondence: juan.mora@dimme.uhu.es; Tel.: +34-959-217-322

Abstract

Background: Bone tissue engineering has emerged as a promising technique for treating bone defects in large bones. Recent methods have enabled scaffold designs based on predefined microstructures or mechanical behavior patterns, including porosity-graded scaffolds adaptable to heterogeneous load states. However, there is no consensus on the optimal scaffold design strategy, which is sometimes chosen based on the intact bone or results from computational or in vivo experiments. **Objective**: This work proposes the design of graded-porosity triply periodic minimal surface (TPMS) scaffolds that mimic the mechanical environment within a bone transport callus at the peak of bone tissue production, according to in vivo load measurements. **Methods**: Finite element models based on computational tomography scans were used to define the strain field of the callus at the peak of bone tissue production. The developed scaffold models were evaluated through finite element simulation. **Results**: The callus simulations reported that the period in which maximum woven bone tissue production was achieved corresponds to the period of maximum axial strain. The graded-porosity scaffolds simulated demonstrated their ability to replicate this strain field along the callus. The microstructural parameters and strain environment of the proposed graded-porosity scaffolds were consistent with finding from studies assessing the influence of different microstructural parameters or strain conditions on bone ingrown within scaffolds. **Conclusions**: The proposed approach—designing graded-porosity scaffolds based on the callus strain field at the peak of bone tissue production—proved to be appropriate and may help improve future clinical applications.

Keywords: bone tissue engineering; bone defect; graded-porosity scaffolds; bone transport; FEM based on CT

Academic Editor: Ugo D'Amora

Received: 20 January 2026
Revised: 13 February 2026
Accepted: 5 March 2026
Published: 9 March 2026

1. Introduction

In bone tissue engineering (BTE), it is widely accepted that scaffolds must facilitate bone growth by enabling cell and tissue strains that generate optimal mechanical signals for ossification. Experimental evidence indicates that the geometry of a given porous scaffold strongly influences cellular responses and can accelerate bone regeneration [1–3]. In this context, several scaffold design parameters—such as pore size and shape, stiffness,

topology or surface-area-to-volume ratio (SSA)—significantly influence the bone regeneration process [4]. Regarding porosity and pore size, the minimum requirement for pore size is approximately 100 μm due to cell size, migration requirements and transport. Pore sizes exceeding 300 μm are commonly used in vivo, as this facilitates vascularization and bone ingrowth [5]. It is also accepted that scaffolds should have distributed and interconnected pores to ensure cell penetration, vascular ingrowth, nutrient diffusion, and waste removal [6]. Triply periodic minimal surface (TPMS) scaffolds meet these requirements through a relationship between porosity and stiffness levels [7]. These scaffolds are manufactured by 3D printing from the design of a repeatable unit cell [8].

The design of scaffolds remains an active area of research, as experimental studies have yielded contradictory results regarding design parameters and materials used. For example, some authors reported no notable effect in bone growth for scaffolds with a larger SSA in vivo [9]. Furthermore, different materials are currently in use, such as titanium [10], printable polymers [6-7] or bioceramics [11,12]. The scaffold design process also relies on computational models, which have been used to predict the strain field within the scaffold for different design parameters [11] and to estimate the fluid-mechanical conditions around it [6]. Recently, more complex agent-based models have been employed to predict the formation of bone tissue according to different design parameters [13,14].

In the case of the treatment of critical bone defects, the use of 3D-printed scaffolds is a promising alternative treatment with advantages over more usual treatments such as bone graft or bone transport. When distraction osteogenesis is applied in bone transport [15], risks related to viscoelastic and structural changes in the surrounding soft tissues arise [16]. Regarding bone substitutes, autografts and allografts have certain disadvantages such as the possibility of rejection and limited availability [17,18]. The increasing number of trauma patients with long-bone defects is increasing global demand [19]. However, scaffolds for large-defect correction are still to be adopted in clinical practice [20]. Beyond finding suitable materials and optimal SSAs, correcting critical defects remains a major challenge. A scaffold for this application must provide sufficient mechanical stability to the limb while still allowing strains within the range required to generate optimal mechanical signals for ossification. There is evidence in the literature that the optimal scaffold geometry for treating critical bone defects can be estimated from the strain field of intact bone [11,21]. However, the mechanical properties of the callus, which is softer and more heterogeneous than intact bone, vary throughout the bone regeneration process [15,22,23]. Consequently, defining a mechanical strain reference for scaffold manufacturing is challenging.

Recent studies based on computational models and experiments found that the scaffold surface guides cellular migration and tissue formation processes, and that the scaffold material composition stimulates cell activity. According to the works of Perier-Metz and coworkers [13,14], a lower scaffold SSA was beneficial for bone regeneration due to enhanced cellular migration, contrary to what has been reported by previous experimental work [10]. They also observed that scaffolds with lower apparent elastic modulus favored bone formation. These conclusions are for a particular case of bone defect, 3 cm sheep tibiae, and scaffold: a 3D-printed strut-based composite biomaterial scaffold (80% medical-grade polycaprolactone mixed with 20% tricalcium phosphate). Despite their sophistication, such models have only been validated under specific conditions. Therefore, these results must not be generalized to scaffold designs intended for critical-defect correction. For example, this model does not consider the use of gradient porosity scaffolds. Previous studies [5] have recommended gradients in pore sizes for research focused on the formation of multiple tissues and tissue interfaces, such as in the case of a healing callus. Current fabrication techniques, such as 3D printing, can be used to generate scaffolds with

morphological and mechanical properties designed to meet the specificity of bone repair [5].

3D-printed TPMS-graded porous scaffolds have been studied for treatment of bone defects due to their higher versatility to adapt to the properties of biological materials [24]. Methods have been developed to generate anisotropic BTE scaffolds with graded structures that can adapt to various requirements in the evolution of porosity [25–27] including mechanobiology-driven optimization algorithms [28–30]. Yang and coworkers [31] reported promising experimental results in mandible augmentation using graded porous scaffolds versus scaffolds with uniform porosity. Despite important advances in possibilities of design and production, several factors still prevent the clinical application of graded porous scaffolds in humans. One major challenge is the difficulty in defining a mechanical reference for scaffold behavior during the design process. For example, Liu and coworkers [26] established natural cortical bone as reference. Other proposed mechanobiology-driven optimization algorithms [25,27] did not define a pattern for the scaffold design in terms of mechanical strain, depending on the clinical application.

Currently, technology is available to manufacture variable-porosity scaffolds, as well as algorithms to define the geometrical parameters of the scaffold based on the mechanical behavior and strain level, which is expected, but what is the optimal strain level for a scaffold?

This study explores and applies a simpler strategy for designing BTE scaffolds with graded morphological and mechanical properties to defect correction, based on experimental data. We hypothesize that, for the treatment of large-bone defects requiring fixation devices, the strain field within the scaffold should mimic that within the callus at the moment of maximum bone tissue production, as observed in alternative bone regeneration processes used to treat the same defect without a scaffold. In a callus without a scaffold, the production of woven bone occurs over the previously generated woven bone, which functions as a scaffold. It is known that during the bone regeneration process, there is a moment when the production of new bone reaches its maximum [15]; the base structure of woven bone (scaffold) provides an optimal foundation for the deposition of new bone, facilitating ossification.

Therefore, in this study, it is assumed that the strain environment corresponding to maximal woven bone production reflects an optimal mechanical target for the skeletal system. The average axial strain within the callus during bone regeneration for a 15 mm critical-size defect in a sheep metatarsus treated with bone transport was analyzed computationally using computational tomography (CT)-based models. Different models of TPMS scaffolds with graded porosity and appropriate dimensions to cover the same initial 15 mm defect were designed and simulated using real boundary conditions measured during the alternative regeneration process in vivo. The goal was to obtain a final scaffold, suitable for 3D printing, whose average axial strain and elastic modulus resemble those of the distraction callus at the moment of maximum bone tissue production.

2. Materials and Methods

2.1. Evolution of the Strain Within the Callus Based on Experiments

An experiment on bone transport was conducted in the metatarsus of 11 female merino sheep, body weight 53.5 ± 8.5 kg, in a previous work [15] to correct a 15 mm defect. The bone transport process consisted of a latency phase of 7 days after surgery, in which the distractor was implanted, and a distraction period of 15 days, during which the bone segments were separated by 1 mm per day. The consolidation phase then continued until distractor removal, which occurred 153 ± 44 days after surgery. Once the callus was totally ossified and the distractor was removed, bone remodeling continued. In a previous study, the authors reported the evolution of callus stiffness using finite element (FE) models

https://doi.org/10.3390/prosthesis8030028

based on CT images acquired at multiple healing time points [23]. These time points included 17, 22, 29, 35, 37, 50, 79, 98, 137, 161, 205, 277, 311, 379, and 471 days after surgery. The models include the callus and adjacent cortical bone segments (Figure 1). They were subjected to real axial loads through the callus, measured during gait in vivo [15], at the proximal end and fixed at the distal end. Table 1 shows the loads applied through the callus at each simulation time point. Different methods to assign mechanical properties were used. The method based on the level of Hounsfield Units of the CT scans provided predictions of callus stiffness more in concordance with in vivo experiments. In this study [23], the objective was to quantify the evolution of callus stiffness, and other parameters of interest, such as the callus strain field, were not analyzed.

The same FE models based on CT images were used here to analyze the evolution of the axial strain and other mechanical parameters within the callus and study their association with the production of woven bone during the bone transport process. First, the production of woven bone over time was evaluated by deriving the equation governing callus volume evolution with time proposed by [15]. Second, the axial strain was evaluated in different regions of the callus to detect any repeating pattern in the local variation in callus strain. The FE simulations were run on ABAQUS® (Dassault Systèmes Simulia Corp., Johnston, RI, USA). C3D4 tetrahedral elements were used with dimensions on the order of the resolution of the CT images (200 to 300 μm/voxel). Material properties were defined as linear elastic, with the elastic modulus determined by the level of Hounsfield Units and a Poisson's ratio of 0.3 [23]. The calluses were modeled as continuous solids disregarding porosity; therefore, the simulations reported average strain in a voxel-size volume. The local microscale strain distribution cannot be simulated with this model and is not within the scope of this study. Table S1 is included in the Supplementary Materials to provide details of all the FE models based on CT images of the callus: number of elements, volume of the model, average volume and reference length per element.

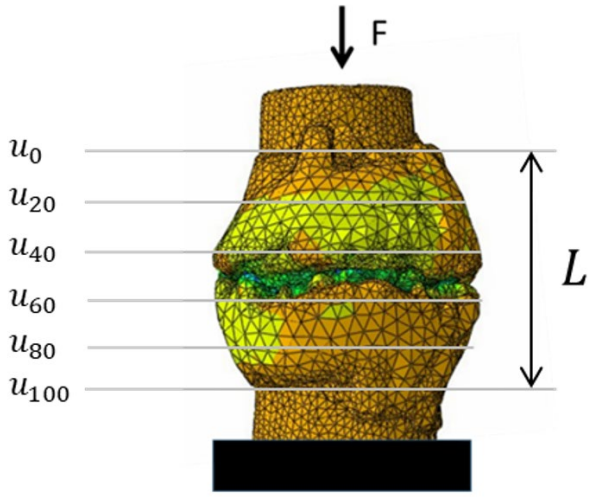

Figure 1. Finite element model based on CT images of the callus taken 50 days after bone transport surgery. Reference points to calculate the mean axial displacement at 0%, 20%, 40%, 60%, 80% and 100% of the callus length from proximal to distal are shown.

Table 1. Load through the callus, applied during the simulation, according to each time point. Note that more time since surgery does not always mean more force, as different time points correspond to different animals with varying body weights [23].

Days From Surgery	Animal Code	F (N)
17	9	46.6
22	7	107.5

29	8	202.3
35	3	235.9
37	6	339.6
50	11	492.5
79	2	481.9
98	1	687.4
137	10	611.5
161	4	694.9
205	10	615.9
277	5	615.9
311	10	615.9
379	5	455.8
471	5	455.8

2.2. Finite Element Model of Scaffolds with Graded Porosity

Several sheet-type TPMS scaffold models with longitudinal graded porosity—Shoen Gyroid (SG) ranging from 60 to 80%, 65 to 85%, and 70 to 90%—were designed with dimensions matching the original defect (a cylinder 15 mm in diameter and 15 mm in length). SG structures were chosen as they have demonstrated consistent biomechanical behavior in BTE applications in recent studies [32–34].

All scaffolds were designed using LisbonTPMS-tool [35], a Python package dedicated to the design of TPMS structures with user-defined resolution. Volume fraction/porosity control is achieved by the common level-set method [36,37], where a mathematical offset is applied to a 3D grid, generating a 3D volume. Tetrahedral meshes were generated from triangular meshes using the MMG3D anisotropic tetrahedralization algorithm [38].

The LisbonTPMS-tool package allows for the generation of custom gradient profiles, with a simple linear example present in Figure 2a. C3D4 tetrahedral elements (Figure 2c) were used with linear-elastic mechanical properties (E = 1460 MPa; υ = 0.3) consistent with the capabilities of the MJP 3600® MultiJet printer (3D Systems, Rock Hill, SC, USA) and the commercial material Visijet M3 Crystal [6]. Since these scaffolds are periodic and have the same geometry at each transverse plane, simulations were applied to a representative cylindrical model with the same length but a smaller surface area (SA) (cylinder: 4.2 mm diameter, 15 mm length; Figure 2b) to save computational cost. Load and boundary conditions were set according to the callus models [23]: axial load at the proximal end and nodes fixed at the distal end. Load was determined according to the alternative regeneration process in vivo [15], using the force through the callus during the maximum ossification period, F, as reference. This force was scaled, F· s/S, depending on the SA of the representative model relative to the appropriate dimensions of the scaffold to cover the same initial defect (Figure 2b).

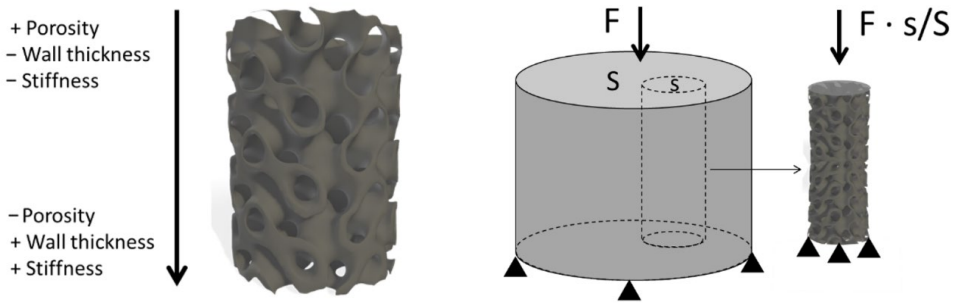

(**a**) (**b**)

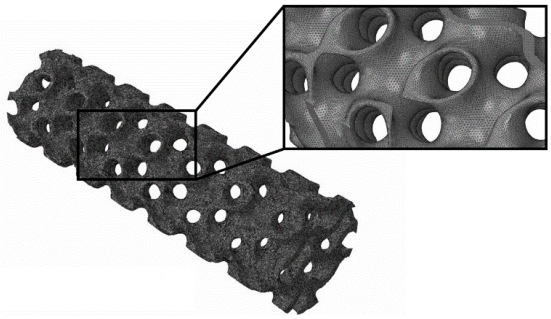

(**c**)

Figure 2. (**a**) Example of a scaffold with linearly variable porosity generated with the method described. (**b**) Representative model of the scaffold for simulations. F is the force applied to the callus during the maximum ossification period, S is the surface of the original scaffold model, and s is the surface of the representative model. (**c**) Images of the mesh of the representative model of the scaffold SG6080 for simulations.

Apart from the controlled porosity configurations, all scaffolds were generated considering a cell size of 2.14 mm. This value was chosen so that the pore size distribution (PSD) of the considered lattice (SG)—for the considered range of porosities, 60–90%—was over the 300 μm mark. The PSD was analyzed using the local thickness method developed by Hildebrand and Rüegsegger [39], implemented and available at PoreSpy [40]. Figure 3 presents the PSD of SG lattices with 60% and 90% porosity, shown as both probability density and cumulative density functions (cfd and pfd respectively).

It should be noted that the scaffold models have a complex geometry that accurately reflects the microstructure (Figure 2c). However, the calluses were modeled as continuous solids (Figure 1), disregarding porosity and assigning the mechanical properties of each element based on the gray level. Consequently, the number of elements in the scaffolds models is higher. Table S2 is included in the Supplementary Materials to provide details of all the FE scaffold models used in this work: number of elements, volume of the model, average volume and reference length per element. The difference in structural scale between the callus and scaffold models does not affect the comparison of average strains, as these values are computed over solid domains that are substantially larger than the underlying microstructure, as is explained in the Results section.

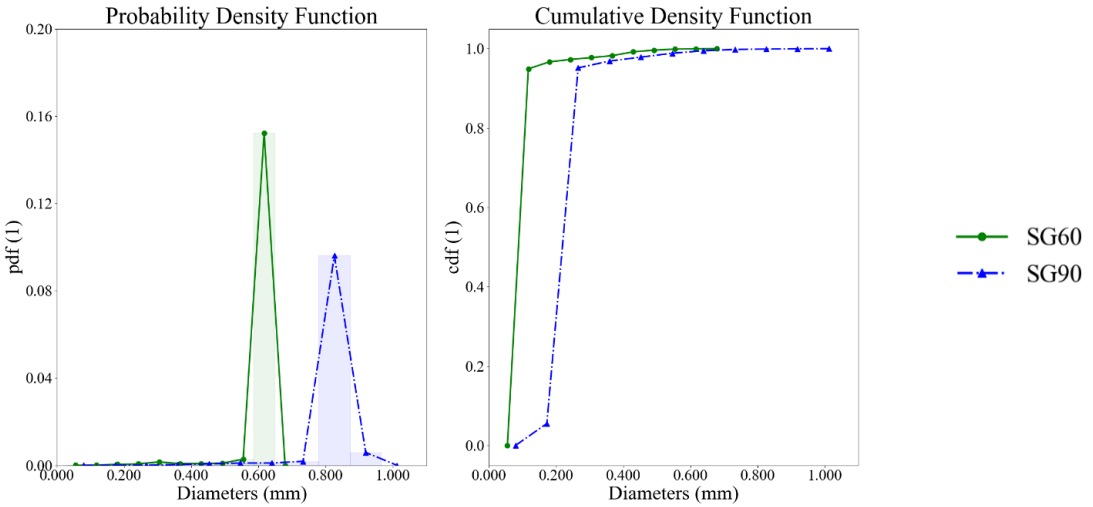

Figure 3. Probability, pdf(1), and cumulative density function, cdf(1), of the SG lattices with 60 and 90% porosity, considering a cell size of 2.14 mm.

3. Results

3.1. Distribution of Callus Strain During the Peak Ossification Period

By deriving the equation that describes the evolution of callus volume during bone transport [15], it can be seen that the maximum rate of woven bone production (0.146 cm^3/day) occurs between 25 and 60 days after surgery (Figure 4). After this peak, woven bone production becomes negative around 100 days after surgery due to remodeling activity.

The average axial strain within each simulated callus model is also represented in Figure 4. The total average strain was estimated as the difference between the mean displacements at the ends of the callus, $u_{100} - u_0$, divided by the length of the callus, L (Figure 1). It may be observed that the maximum ossification period occurs at the maximum strain within the callus (Figure 4). During this time, 29 to 50 days after surgery, the average callus strain varied between 0.010 and 0.035. Outside this time period, the average strain did not exceed 0.0038. Focusing on the local evolution of the strain, it is clearly observed that axial strain increases in the center of the callus during the maximum ossification period (Figure 5). This figure represents the average strain within the callus at different longitudinal points (10%, 30%, 50%, 70% and 90% of the callus length from proximal to distal; see Figure 1) for all models from 17 to 525 days post surgery. Calluses within the maximum ossification period (29, 35, 37, and 50 days post surgery) generally presented higher strain values compared to the other specimens, with peak strains occurring near the center of the callus. In this region, strain values can be more than twice as high as those at the proximal and distal ends. No repeated trend in the longitudinal evolution of strain was observed in the callus at time points outside the maximum ossification period. These average strain values in Figure 5 were calculated from the axial displacement at nodes, as indicated by Equations (1)–(5). In these equations, $\epsilon_{X\%}$ represents the average axial strain at *X*% of callus length, measured from proximal to distal. This is based on mean displacement at *X* − 10% (u_{X-10}) and *X* + 10% (u_{X+10}) of the callus length and the original length of this segment, L/5. The mean displacements, u_0, u_{20}, u_{40}, u_{60}, u_{80}, and u_{100}, were obtained as the mean axial displacements of nodes in the callus model around 1mm of the position points, 0%, 20%, 40%, 60%, 80% and 100% of the callus length, from proximal to distal (see Figure 1).

$$\epsilon_{10\%} = \frac{u_0 - u_{20}}{L/5} \quad (1)$$

$$\epsilon_{30\%} = \frac{u_{20} - u_{40}}{L/5} \quad (2)$$

$$\epsilon_{50\%} = \frac{u_{40} - u_{60}}{L/5} \quad (3)$$

$$\epsilon_{70\%} = \frac{u_{60} - u_{80}}{L/5} \quad (4)$$

$$\epsilon_{90\%} = \frac{u_{80} - u_{100}}{L/5} \quad (5)$$

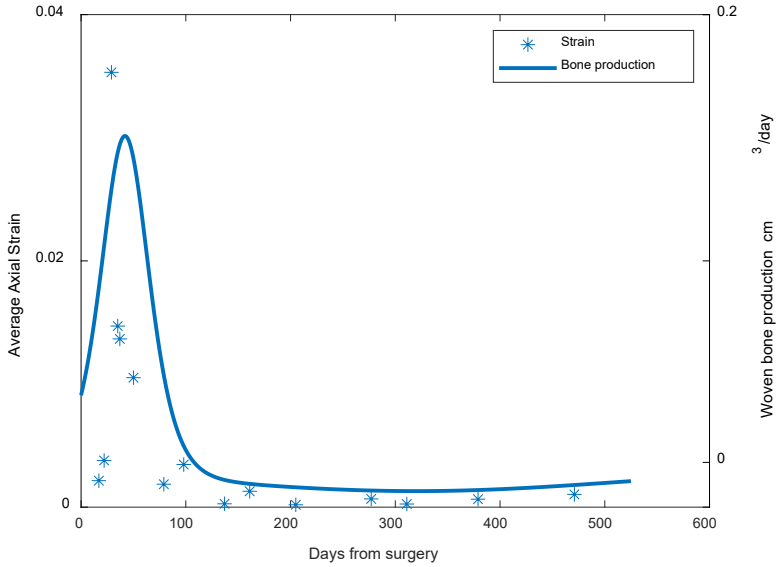

Figure 4. Evolution of woven bone production and the average axial strain within a bone transport callus.

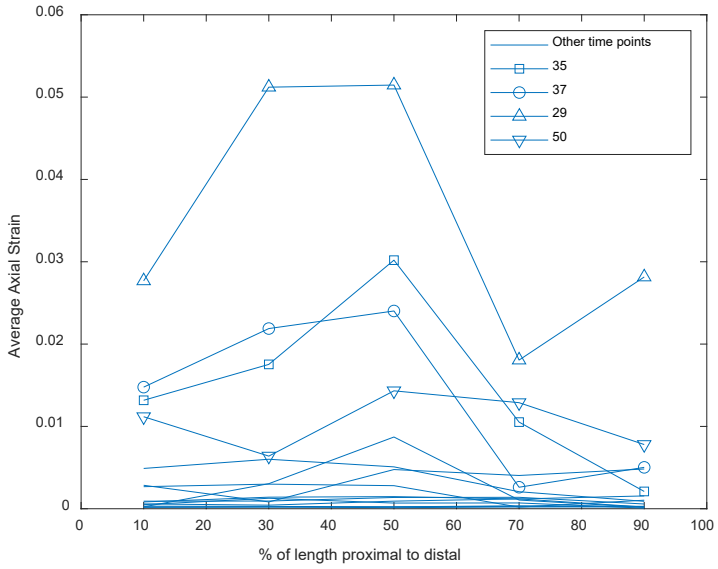

Figure 5. Longitudinal evolution of average callus strain from proximal to distal.

The average strain within the callus at different longitudinal points is depicted using Whisker diagrams in Figure 6 for specimens during the maximum ossification period. It can be observed that, during this period, the axial strain around the callus peaks in the middle, with a median value of 0.027, and is lower at the ends, with median values of 0.0140 and 0.0064 at the proximal and the distal ends respectively. The average elastic modulus of these specimens is also shown in the same figure, with a median value of 115.71 MPa. The average elastic modulus was calculated as the average stress over the callus at each time point divided by the total average strain. The average stress was obtained by dividing the applied force at each time point (Table 1) by a normalized callus area. Having established both the average elastic modulus and the longitudinal evolution of axial strain during the maximum ossification period, the next objective is to design a graded porous scaffold with comparable mechanical properties.

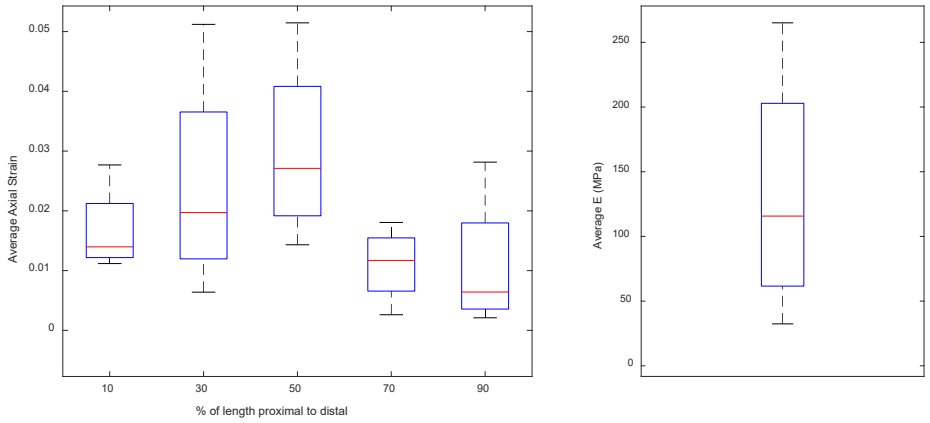

(**a**) (**b**)

Figure 6. Whisker box plot summarizes the distribution of the different parameters measured as results of the simulations of the four calluses within the maximum ossification period (29, 35, 37 and 50 days after surgery): (**a**) the average axial strain within the callus at different longitudinal points from proximal to distal; (**b**) the average elastic modulus. Whisker box plot represents the median (50th percentile of the data, red line inside the box), the first quartile (25th percentile, lower boundary of the box), the third quartile (25th percentile, upper boundary of the box), and the high and low observations relative to the rest of the dataset (individual points plotted beyond the box).

No consistent strain pattern was observed locally in the transverse directions of the callus (anterior to posterior or medial to lateral). This finding agrees with previous studies that do not show a repeated pattern of variation in the mechanical properties of the woven bone within the callus during the bone transport process [22].

3.2. Strain Distribution of Graded Porous Scaffolds

The average axial strain within the graded porous scaffolds proposed was evaluated at the same longitudinal positions as the callus (10%, 30%, 50%, 70% and 90% of the scaffold length from proximal to distal). The strain calculation methods at these locations were identical to those used for the callus models. Considering the longitudinal evolution of the callus strain, four TPMS scaffold models were initially proposed as proof of concept, featuring different geometries and linear variations in the porosity, with maximum porosity at the ends and minimum porosity at the center (Table 2). Table 3 shows mean structural properties of the mentioned designed models.

The simulation results were plotted together with the callus strain in the same graph (Figure 7). As shown in Figure 7a, the strains of models SG6585 and SG7090 are in the order of the strain at the ends of the callus: 0.01 to 0.02. The SG7090 scaffold is significantly softer in the middle. In contrast, models SG6080 and SG6585 show mechanical behavior closer to that of the callus center, with strain values between 0.02 and 0.04. In any case, a symmetrical porosity variation does not properly represent the axial strain variation along the callus, which is greater at the proximal end. Regarding the average elastic modulus (Figure 7b), all the scaffolds present an average elastic modulus between the 25th and 75th percentile of the average elastic modulus of the callus. However, the average elastic modulus of SG7090 seems too far away from the average values of the average elastic modulus of the callus.

Table 2. Models of graded porous scaffolds initially simulated.

Model	Type of Geometry	Porosity at the Ends	Porosity at the Center
SG6080	Gyroid	60%	80%
SG6585	Gyroid	65%	85%
SG7090	Gyroid	70%	90%

Table 3. Properties of graded porous scaffolds initially simulated.

Model	Type of Geometry	Volume (mm^3)	SA (mm^2)	SSA (mm^{-1})
SG6080	Gyroid	62.29085	671.05987	10.77301
SG6585	Gyroid	51.88499	668.10217	12.87660
SG7090	Gyroid	41.58436	667.10156	16.04211

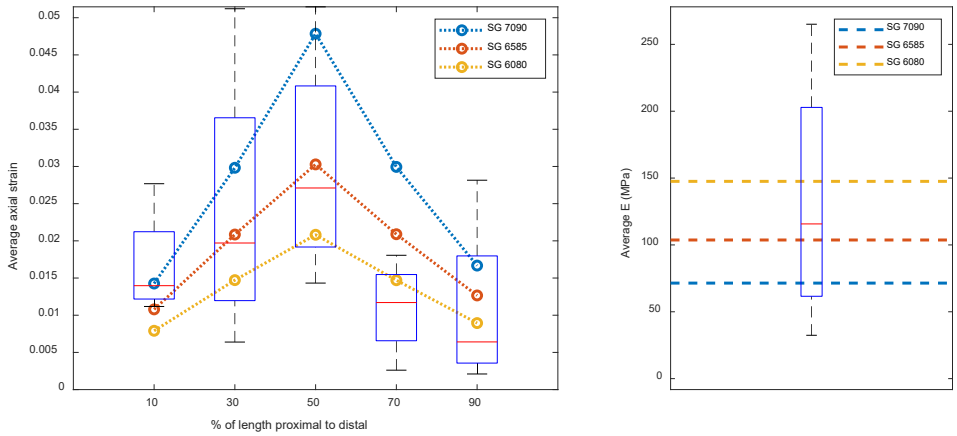

(**a**) (**b**)

Figure 7. (**a**) Average axial strain at different longitudinal location points from proximal to distal: for the callus at the maximum ossification period (Whisker boxes) and for the scaffolds (SG7090, SG 6585 and SG6080). (**b**) Average elastic modulus of the callus at the maximum ossification period (Whisker box) and the scaffolds.

3.3. Optimum-Graded Porous Scaffolds That Mimic Callus Strain Distribution

Based on the outputs above, two non-symmetrical SG scaffold models with variable porosity were proposed, as detailed in Table 4. These models use SG7090 porosity at the proximal end, SG6585 at the center, and SG6080 at the distal end, resulting in different porosity patterns changing from 70 (proximal) to 85% and then to 62.5% (distal). The longitudinal evolution of the average axial strain in these proposed models aligns with the trend observed in the callus during the peak ossification period (Figure 8a). The average elastic modulus is aligned with the mean value for the callus at the maximum ossification period (Figure 8b). Table 5 shows the mean structural properties of the optimized models.

Table 4. Optimum models of graded porous scaffolds, Gyroid geometry, with linear variable porosity between reference points along the length from proximal to distal (10, 30, 50, 70 and 90%).

Model	Porosity at 10%	Porosity at 30%	Porosity at 50%	Porosity at 70%	Porosity at 90%
SG 70, 77.5, 85, 65, 62.5	70%	77.5%	85%	65%	62.5%
SG 70, 75, 85, 67.5, 62.5	70%	75%	85%	67.5%	62.5%

Table 5. Structural properties of the optimized models.

Model	Volume (mm³)	SA (mm²)	SSA (mm⁻¹)
SG 70, 77.5, 85, 65, 62.5	58.209	603.32	10.36
SG 70, 75, 85, 67.5, 62.5	58.229	603.68	10.37

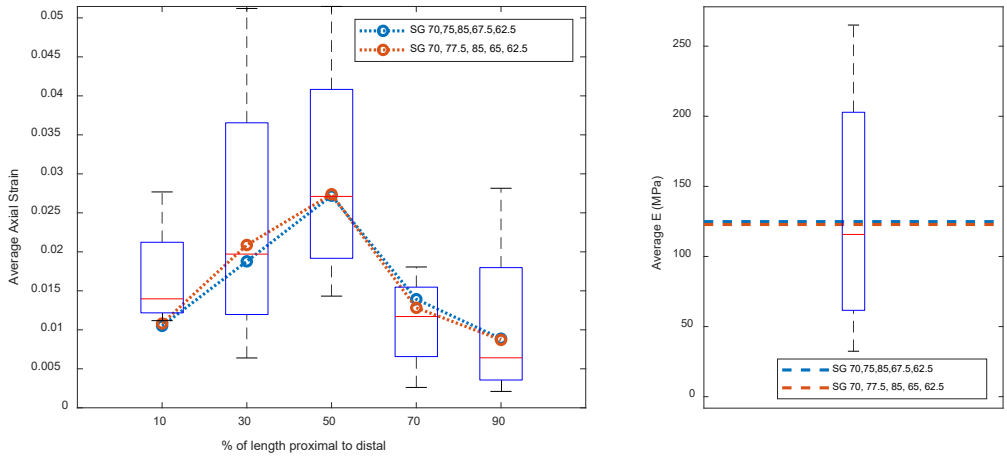

Figure 8. (**a**) Average strain at different longitudinal points from proximal to distal: for the callus at the maximum ossification period (presented by Whisker boxes) and the optimal scaffold models (SG 70, 75, 85, 67.5, 62.5 and SG 70, 77.5, 85, 65, 62.5). (**b**) Average elastic modulus of the callus at the maximum ossification period (Whisker box) and the optimal scaffolds.

4. Discussion

This study analyzed the temporal and longitudinal evolution of strain within a distraction callus to address a 15 mm defect during a previous bone transport experiment conducted on sheep [15,23]. The results showed that the period of maximum woven bone production coincided with the period of maximum axial strain within the distraction callus (Figure 4). Therefore, it may be assumed that this level of strain along the callus optimizes the production of woven bone over the previously mineralized bone of the callus. Based on this hypothesis, a scaffold designed for an equivalent defect using BTE should reproduce the strain field present in the callus at the moment of maximum bone tissue production. It has also been demonstrated that, at this time point, the strain along the callus is variable (Figure 6a) and therefore not reproducible by uniform microstructure scaffolds. Simulations performed on two non-symmetrical TPMS scaffolds with Gyroid geometry showed that these designs can mimic the average axial strain within the distraction callus at the moment of maximum bone tissue production (Figure 8a). The proposed models are consistent in stiffness with the average elastic modulus of the callus at the maximum ossification period (Figure 8b). Designing scaffolds that mimic the woven bone strain field at the stage of maximum tissue production represents a novel approach, especially given that the parameters guiding scaffold design are still under investigation.

Compared with conventional lattices, TPMS-based scaffolds offer improved mechanical performance and higher SSA values. They are increasingly studied for BTE applications, especially in load-bearing scenarios [26,29,41]. The structural features that compose a lattice structure (porosity and cell size) were calculated based on the target mechanical behavior. This was achieved by applying a graded porosity profile to the scaffold and adjusting it to match the stress–strain distribution of the woven bone. The resulting porosity values, combined with the selected cell size, produce a fully percolative structure with high SSA and pore sizes suitable for biofluid infiltration and effective cell seeding.

This represents a valuable contribution to the development of custom-graded scaffolds for treating large-bone defects. As far as the authors know, there are no other works in the literature demonstrating this fine-tuning of a gradient structure in order to follow a target behavior for scaffolds in large-bone-defect applications.

The outcomes obtained were consistent with recent studies that explored the influence of scaffold design in large-bone-defect regeneration using various methods. The optimal graded-porosity scaffold shows an average elastic modulus of 124.8 MPa, which falls within the 32.4–265 MPa range reported for woven bone during the peak ossification period (Figure 8b). Although some in vivo studies have used much stiffer scaffolds—such as bioceramic scaffolds with an average elastic modulus of 9.54 GPa for a 15 mm defect in sheep [12] or titanium scaffolds with moduli of 0.84 and 2.88 GPa for a 40 mm defect [10]—more recent work suggests that scaffold compliance enhances bone regeneration. Perier-Metz and coworkers [13,14] predicted optimal bone growth in 30 mm defects using scaffolds with an average elastic modulus of 70 MPa, outperforming both stiffer (400 MPa) and softer (0.1 MPa) scaffolds in a computational model partially validated in vivo. Reznikov and coworkers [42] conducted an in vivo study on sheep femurs with the same defect size used here (15 mm). They found that compliant polyamide scaffolds with an average elastic modulus of 220 MPa produced greater bone ingrowth after six weeks than stiffer titanium scaffolds with moduli of 1400 and 7100 MPa. In addition, 22.2 MPa β-tricalcium phosphate was used for a 30 mm defect in sheep tibiae [43]. Concerning the porosity of the scaffold, the optimal graded-porosity models ranged from 62.5 to 85% (Table 4) with variable pore diameter around 0.4 to 0.8 mm (Figure 3). Different values of porosity and pore size were proposed for uniform porosity scaffolds used in vivo: 59.3% porosity and pore size around 360 μm [12]; 70% porosity and pore size around 1200 μm [43]. The studies which have analyzed the potential in bone ingrowth of different geometries also provided mixed results for the porosity and pore size that enhance bone regeneration, e.g., 60% porosity and pore size around 1000 μm [13,14] or 35% porosity [42]. In fact, a previous work in which scaffolds of different pore sizes were implanted subcutaneously in immuno-compromised mice [9] concluded that pore sizes between 350 and 800 μm play a limited role in bone ingrowth in this tissue engineering model. A similar situation occurs with SSA: while bioceramic scaffolds showed an SSA of 5.7689 mm^{-1} [12], other studies observed much higher values (31–278 mm^{-1}) [13,14] and reported that lower SSAs enhanced bone ingrowth, contradicting earlier findings [10]. In the case of the proposed optimized models, SSA values are around 10–13 mm^{-1}. The strain levels during the peak ossification period in bone transport—which the optimized scaffolds aim to reproduce—range from 0.005 to 0.05. Saving the differences among studies, this is comparable to the strain within scaffolds that promote optimal bone regeneration, as observed in studies examining the impact of scaffold design on large-bone-defect regeneration and reporting strain field data [13,14]. Note that the scaffold design parameters discussed in this paragraph are for scaffolds manufactured with different materials, fabrication techniques and animal models, hindering direct comparison. However, by focusing on in vivo experiments and in silico models validated with in vivo data, this work enables meaningful comparison of how different scaffold geometries influence bone growth.

The method developed here to define scaffold porosity is based on mimicking the strain field in woven bone under real loads (functional biomimetism), rather than replicating the natural bone microstructure as proposed in other graded-porosity scaffold designs [4]. Although the goal was not to replicate bone microstructure, the optimal graded-porosity models show microstructural properties partially consistent with woven bone during maximum tissue production (35–50 days after surgery in the referenced sheep metatarsus model). Previous studies in a similar animal model reported that average porosity of the woven bone within the distraction callus, estimated from bone volume versus total

volume micro-CT measurements, was around 60% [44] versus 62.5 to 85% for the optimal model proposed here (Table 4). Micro-CT analysis of woven bone at the same stage and in the same model reported trabecular thickness and separation of 0.1–0.2 mm [44], which is smaller than the pore sizes of the proposed scaffolds (above 0.5 mm; Figure 3). This generates controversy and, as far as the authors know, it has not been experimentally proven which factor plays a more important role in bone ingrowth: the geometry of the microstructure on which the new bone tissue develops or the mechanical environment to which said structure is subjected. In any case, future work could expand on this by designing scaffolds that replicate specific mechanical behaviors and microstructures. A significant improvement could be the use of materials with mechanical properties similar to those of woven bone at the desired stage. This is a challenge since such materials would also have to comply with 3D printing techniques required to manufacture variable-porosity scaffolds. In fact, for the optimal scaffold proposed here, there is a difference between the woven bone elastic modulus (3 to 10 GPa [22]) and the elastic modulus of this scaffold material (1.460 GPa). It should be noted that the porosity distribution obtained from the optimization process would differ if a different scaffold material were used. The scaffold material is stiffer than woven bone. This could imply potential fatigue or long-term mechanical integrity issues, which are beyond the scope of this study but should be considered in future work.

This work presents a useful and agile method to produce scaffolds based on mimicking the mechanical environment during defect ossification. This method saves time and resources compared with heavier mechanobiological computational models [13] but needs to be validated through in vitro or in vivo studies. Another limitation of the present work is the difference in scale between the scaffold and callus models. Although this structural mismatch does not affect the comparison of average strains, it does not allow for studying the effect of other parameters, such as strain energy density, different components of the strain tensor, and maximum and minimum strain, in the production of woven bone. Therefore, a characterization of the callus mechanical environment at a smaller scale is necessary, for example, through FE models based on micro-CT scans of the callus.

Beyond the limitations discussed above, additional considerations must also be acknowledged. In this study, the scaffold design is focused solely on mimicking the mechanical macroscopic average strain field corresponding to maximal woven bone production. However, it is important to recognize that woven bone deposition is also shaped by a range of biological factors, including cellular activity, inflammatory signaling, vascularization, and tissue-level constraints. In addition, fluid movement within the pores may influence the local strain experienced at the surface of the woven bone/scaffold, thereby affecting the ossification process. These fluids within pores should not alter the strain values reported here, as they represent the average deformation of a comparatively large volume. Our interpretation of macroscopic strain patterns as optimal should therefore be understood within a broader framework in which solid- and fluid-mechanical environments interact with biological drivers to guide bone adaptation. Future research should further investigate the relationships between macroscopic and local mechanical environments and the biological responses that shape bone tissue engineering outcomes. In addition to the limitation associated with other factors that also contribute to new bone formation, it should be noted that the reference strain reported in this work (during the period of maximum bone tissue production) may vary depending on the individual, the specific bone involved, its intrinsic properties or variations to the boundary conditions assumed for simulating.

As final remarks, there are methods to design BTE scaffolds capable of defining geometrical properties to achieve a predefined mechanical behavior [21]. However, defining

the mechanical behavior patterns required in bone regeneration remains challenging, especially when the scaffold must fulfill both structural and osteoconductive functions. This study explored the hypothesis that the axial strain pattern within a bone callus of a given length can serve as a template for defining the mechanical environment of a scaffold designed to treat a defect of the same length. The analyses of the callus axial strain revealed that the axial strain of the woven bone within the callus follows a longitudinal variable trend along the scaffold. The approach used in this study, to generate variable-porosity TPMS scaffolds, provided a pair of models with microstructures which may replicate the evolution of the axial strain within the woven bone at the maximum-tissue-production time point. This strategy—using the woven bone strain field during maximum tissue production as a design pattern—may help guide recently developed scaffold design methods and mechanobiology-based algorithms for optimizing graded-porosity scaffolds [25,26,28–30].

Supplementary Materials: The following supporting information can be downloaded at https://www.mdpi.com/article/10.3390/prosthesis8030028/s1. Table S1 provides details of all the FE models based on CT images of the callus used in this work: number of elements, volume of the model, average volume and reference length per element. Table S2 provides details of all the FE scaffold models used in this work: number of elements, volume of the model, average volume and reference length per element.

Author Contributions: J.M.-M. and P.R.F.: conceptualization, supervision, project administration; J.M.-M. and J.E.S.: data curation, methodology, software; J.M.-M., P.R.F. and A.P.G.C.: validation, formal analysis; J.M.-M. and J.E.S.: visualization; J.M.-M. and J.E.S.: writing—original draft; J.M.-M., P.R.F. and A.P.G.C.: funding acquisition; J.M.-M., J.E.S., A.P.G.C. and P.R.F.: writing—review and editing, investigation, resources. All authors have read and agreed to the published version of the manuscript.

Funding: J.M.-M. is grateful for the support of the MICIU (Ministry of Science, Innovation and Universities of the Spanish Government) and ERPF/EU (European Regional Development Fund of the European Union) via Grant PID 2023-148828OB-I00 funded by MICIU/AEI/10.13039/501100011033 and by the ERDF/EU. J.E.S., A.P.G.C. and P.R.F. are grateful to Fundação para a Ciência e a Tecnologia (FCT), Portugal, for its financial support via LAETA (DOI: 10.54499/UID/50022/2025). J.E.S. also acknowledges FCT for the PhD grant UI/BD/150995/2021. Finally, A.P.G.C. and P.R.F. declare that this article is partly based upon work from COST Action EuroCurvoBioNet CA22153, supported by COST (European Cooperation in Science and Technology).

Institutional Review Board Statement: Not applicable. This study uses animal data obtained from previously approved experimental protocols. There are no ethical issues for human and animal rights.

Informed Consent Statement: Not Applicable

Data Availability Statement: Technical details or raw data necessary to replicate this study that are not included in the manuscript or the supplementary material will be made available by the authors upon request, without undue reservation.

Acknowledgments: Authors are grateful for the funding support detailed in the Funding section.

Conflicts of Interest: The authors declare no conflicts of interest.

Abbreviations

The following abbreviations are used in this manuscript:

BTE	Bone tissue engineering.
CT	Computerized tomography
E	Elastic modulus
ϵ	Callus strain
F	Force
FE	Finite element
L	Callus longitude
PSD	Pore size distribution
SA	Surface area
SG	Shoen Gyroid
SSA	Surface-area-to-volume ratio
TPMS	Triply periodic minimal surface
u:	Callus displacement
υ	Poisson ratio

References

1. Bidan, C.M.; Kommareddy, K.P.; Rumpler, M.; Kollmannsberger, P.; Bréchet, Y.J.M.; Fratzl, P.; Dunlop, J.W.C. How linear tension converts to curvature: Geometric control of bone tissue growth. *PLoS ONE* **2012**, *7*, e36336. https://doi.org/10.1371/journal.pone.0036336.
2. Feng, Y.F.; Wang, L.; Li, X.; Ma, Z.S.; Zhang, Y.; Zhang, Z.Y.; Lei, W. Influence of architecture of β-tricalcium phosphate scaffolds on biological performance in repairing segmental bone defects. *PLoS ONE* **2012**, *7*, e49955. https://doi.org/10.1371/journal.pone.0049955.
3. Zadpoor, A.A. Bone tissue regeneration: The role of scaffold geometry. *Biomater. Sci.* **2015**, *3*, 231–245. https://doi.org/10.1039/c4bm00291a.
4. Gómez, S.; Vlad, M.D.; López, J.; Fernández, E. Design and properties of 3D scaffolds for bone tissue engineering. *Acta Biomater.* **2016**, *42*, 341–350. https://doi.org/10.1016/j.actbio.2016.06.032.
5. Karageorgiou, V.; Kaplan, D. Porosity of 3D biomaterial scaffolds and osteogenesis. *Biomaterials* **2005**, *26*, 5474–5491. https://doi.org/10.1016/j.biomaterials.2005.02.002.
6. Pires, T.; Santos, J.; Ruben, R.B.; Gouveia, B.P.; Castro, A.P.G.; Fernandes, P.R. Numerical-experimental analysis of the permeability-porosity relationship in triply periodic minimal surfaces scaffolds. *J. Biomech.* **2021**, *117*, 110263. https://doi.org/10.1016/j.jbiomech.2021.110263.
7. Montazerian, H.; Davoodi, E.; Asadi-Eydivand, M.; Kadkhodapour, J.; Solati-Hashjin, M. Porous scaffold internal architecture design based on minimal surfaces: A compromise between permeability and elastic properties. *Mater. Des.* **2017**, *126*, 98–114. https://doi.org/10.1016/j.matdes.2017.04.009.
8. Hollister, S.J.; Flanagan, C.L.; Zopf, D.A.; Morrison, R.J.; Nasser, H.; Patel, J.J.; Ebramzadeh, E.; Sangiorgio, S.N.; Wheeler, M.B.; Green, G.E. Design control for clinical translation of 3D printed modular scaffolds. *Ann. Biomed. Eng.* **2015**, *43*, 774–786. https://doi.org/10.1007/s10439-015-1270-2.
9. Roosa, S.M.; Kemppainen, J.M.; Moffitt, E.N.; Krebsbach, P.H.; Hollister, S.J. The pore size of polycaprolactone scaffolds has limited influence on bone regeneration in an *in vivo* model. *J. Biomed. Mater. Res. Part A* **2010**, *92*, 359–368. https://doi.org/10.1002/jbm.a.32381.
10. Pobloth, A.-M.; Checa, S.; Razi, H.; Petersen, A.; Weaver, J.C.; Schmidt-Bleek, K.; Windolf, M.; Tatai, A.Á.; Roth, C.P.; Schaser, K.-D.; et al. Mechanobiologically optimized 3D titanium-mesh scaffolds enhance bone regeneration in critical segmental defects in sheep. *Sci. Transl. Med.* **2018**, *10*, eaam8828. https://doi.org/10.1126/scitranslmed.aam8828.
11. Blázquez-Carmona, P.; Sanz-Herrera, J.A.; Martínez-Vázquez, F.J.; Domínguez, J.; Reina-Romo, E. Structural optimization of 3D-printed patient-specific ceramic scaffolds for *in vivo* bone regeneration in load-bearing defects. *J. Mech. Behav. Biomed. Mater.* **2021**, *121*, 104613. https://doi.org/10.1016/j.jmbbm.2021.104613.

12. Blázquez-Carmona, P.; Mora-Macías, J.; Martínez-Vázquez, F.J.; Morgaz, J.; Domínguez, J.; Reina-Romo, E. Mechanics Predicts Effective Critical-Size Bone Regeneration Using 3D-Printed Bioceramic Scaffolds. *Tissue Eng. Regen. Med.* **2023**, *20*, 893–904. https://doi.org/10.1007/s13770-023-00577-2.
13. Perier-Metz, C.; Cipitria, A.; Hutmacher, D.W.; Duda, G.N.; Checa, S. An in silico model predicts the impact of scaffold design in large bone defect regeneration. *Acta Biomater.* **2022**, *145*, 329–341. https://doi.org/10.1016/j.actbio.2022.04.008.
14. Perier-Metz, C.; Duda, G.N.; Checa, S. A mechanobiological computer optimization framework to design scaffolds to enhance bone regeneration. *Front. Bioeng. Biotechnol.* **2022**, *10*, 980727. https://doi.org/10.3389/fbioe.2022.980727.
15. Mora-Macías, J.; Reina-Romo, E.; López-Pliego, M.; Giráldez-Sánchez, M.A.; Domínguez, J. *In Vivo* Mechanical Characterization of the Distraction Callus During Bone Consolidation. *Ann. Biomed. Eng.* **2015**, *43*, 2663–2674. https://doi.org/10.1007/s10439-015-1330-7.
16. Ilizarov, G.A. The principles of the Ilizarov method. *Bull. Hosp. Jt. Dis. Orthop. Inst.* **1988**, *48*, 1–11.
17. Moussa, N.T.; Dym, H. Maxillofacial Bone Grafting Materials. *Dent. Clin. N. Am.* **2020**, *64*, 473–490. https://doi.org/10.1016/j.cden.2019.12.011. Epub 2020 Feb 1. PMID: 32111281.
18. Wickramasinghe, M.L.; Dias, G.J.; Premadasa, K.M.G.P. A novel classification of bone graft materials. *J. Biomed. Mater. Res. Part B Appl. Biomater.* **2022**, *110*, 1724–1749. https://doi.org/10.1002/jbm.b.35029.
19. Sohn, H.S.; Oh, J.K. Review of bone graft and bone substitutes with an emphasis on fracture surgeries. *Biomater. Res.* **2019**, *23*, 9. https://doi.org/10.1186/s40824-019-0157-y.
20. Hollister, S.J.; Murphy, W.L. Scaffold translation: Barriers between concept and clinic. *Tissue Eng. Part B Rev.* **2011**, *17*, 459–474. https://doi.org/10.1089/ten.TEB.2011.0251.
21. Castilho, M.; Rodrigues, J.; Vorndran, E.; Gbureck, U.; Quental, C.; Folgado, J.; Fernandes, P.R. Computational design and fabrication of a novel bioresorbable cage for tibial tuberosity advancement application. *J. Mech. Behav. Biomed. Mater.* **2017**, *65*, 344–355. https://doi.org/10.1016/j.jmbbm.2016.08.036.
22. Mora-Macías, J.; Pajares, A.; Miranda, P.; Domínguez, J.; Reina-Romo, E. Mechanical characterization via nanoindentation of the woven bone developed during bone transport. *J. Mech. Behav. Biomed. Mater.* **2017**, *74*, 236–244. https://doi.org/10.1016/j.jmbbm.2017.05.031.
23. Mora-Macías, J.; Giráldez-Sánchez, M.Á.; López, M.; Domínguez, J.; Reina-Romo, M.E. Comparison of methods for assigning the material properties of the distraction callus in computational models. *Int. J. Numer. Method. Biomed. Eng.* **2019**, *35*, e3227. https://doi.org/10.1002/cnm.3227.
24. Ma, J.; Li, Y.; Mi, Y.; Gong, Q.; Zhang, P.; Meng, B.; Wang, J.; Wang, J.; Fan, Y. Novel 3D printed TPMS scaffolds: Microstructure, characteristics and applications in bone regeneration. *J. Tissue Eng.* **2024**, *15*, 20417314241263689. https://doi.org/10.1177/20417314241263689.
25. Cheikho, K.; Ganghoffer, J.; Baldit, A.; Labbé, E.; Alix, S.; Kerdjoudj, H.; Mauprivez, C.; Lebée, A.; Laurent, C. A flexible design framework to design graded porous bone scaffolds with adjustable anisotropic properties. *J. Mech. Behav. Biomed. Mater.* **2023**, *140*, 105727. https://doi.org/10.1016/j.jmbbm.2023.105727.
26. Liu, F.; Mao, Z.; Zhang, P.; Zhang, D.Z.; Jiang, J.; Ma, Z. Functionally graded porous scaffolds in multiple patterns: New design method, physical and mechanical properties. *Mater. Des.* **2018**, *160*, 849–860. https://doi.org/10.1016/j.matdes.2018.09.053.
27. Zheng, Y.; Huang, C.; Li, Y.; Gao, J.; Yang, Y.; Zhao, S.; Che, H.; Yang, Y.; Yao, S.; Li, W.; et al. Mimicking the mechanical properties of cortical bone with an additively manufactured biodegradable Zn-3Mg alloy. *Acta Biomater.* **2024**, *182*, 139–155. https://doi.org/10.1016/j.actbio.2024.05.023.
28. Boccaccio, A.; Uva, A.E.; Fiorentino, M.; Mori, G.; Monno, G. Geometry Design Optimization of Functionally Graded Scaffolds for Bone Tissue Engineering: A Mechanobiological Approach. *PLoS ONE* **2016**, *11*, e0146935. https://doi.org/10.1371/journal.pone.0146935.
29. Zhang, J.; Chen, X.; Sun, Y.; Yang, J.; Chen, R.; Xiong, Y.; Hou, W.; Bai, L. Design of a biomimetic graded TPMS scaffold with quantitatively adjustable pore size. *Mater. Des.* **2022**, *218*, 110665. https://doi.org/10.1016/j.matdes.2022.110665.
30. Zhang, Z.; Zhang, H.; Li, Y.; Duan, M.; Qin, S.A. Modeling method of graded porous scaffold based on triply periodic minimal surfaces. *Math. Probl. Eng.* **2022**, *2022*, 7129482. https://doi.org/10.1155/2022/7129482.
31. Yang, J.; Kang, Y.; Browne, C.; Jiang, T.; Yang, Y. Graded porous β-tricalcium phosphate scaffolds enhance bone regeneration in mandible augmentation. *J. Craniofacial Surg.* **2015**, *26*, e148–e153. https://doi.org/10.1097/SCS.0000000000001383.
32. Lehder, E.F.; Ashcroft, I.A.; Wildman, R.D.; Ruiz-Cantu, L.A.; Maskery, I. A multiscale optimisation method for bone growth scaffolds based on triply periodic minimal surfaces. *Biomech. Model. Mechanobiol.* **2021**, *20*, 2085–2096. https://doi.org/10.1007/s10237-021-01496-8.

33. Yánez, A.; Herrera, A.; Martel, O.; Monopoli, D.; Afonso, H. Compressive behaviour of gyroid lattice structures for human cancellous bone implant applications. *Mater. Sci. Eng. C* **2016**, *68*, 445–448. https://doi.org/10.1016/j.msec.2016.06.016.
34. Pehlivan, F.; Karamanlı, İ.A.; Temiz, A.; Öztürk, F.H.; Karaca, M.M. Hierarchical cellular structures based on TPMS mimicking cancellous bone. *J. Mech. Behav. Biomed. Mater.* **2025**, *168*, 107037. https://doi.org/10.1016/j.jmbbm.2025.107037.
35. Santos, J.E.; Ruben, R.B.; Fernandes, P.R.; Castro, A.P.G. LISBON TPMS TOOL: An open-source tool for the design of TPMS structures for engineering applications. *Softw. Impacts* **2025**, *24*, 100747. https://doi.org/10.1016/j.simpa.2025.100747.
36. Al-Ketan, O.; Lee, D.W.; Rowshan, R.; Abu Al-Rub, R.K. Functionally graded and multi-morphology sheet TPMS lattices: Design, manufacturing, and mechanical properties. *J. Mech. Behav. Biomed. Mater.* **2020**, *102*, 103520. https://doi.org/10.1016/j.jmbbm.2019.103520.
37. Zhou, X.; Jin, Y.; Du, J. Functionally Graded Scaffolds with Programmable Pore Size Distribution Based on Triply Periodic Minimal Surface Fabricated by Selective Laser Melting. *Materials* **2020**, *13*, 5046. https://doi.org/10.3390/ma13215046.
38. Dapogny, C.; Dobrzynski, C.; Frey, P. Three-dimensional adaptive domain remeshing, implicit domain meshing, and applications to free and moving boundary problems. *J. Comput. Phys.* **2014**, *262*, 358–378. https://doi.org/10.1016/j.jcp.2014.01.005.
39. Hildebrand, T.; Rüegsegger, P. A new method for the model-independent assessment of thickness in three-dimensional images. *J. Microsc.* **1997**, *185*, 67–75. https://doi.org/10.1046/j.1365-2818.1997.1340694.x.
40. Gostick, J.T.; Khan, Z.A.; Tranter, T.G.; Kok, M.D.; Agnaou, M.; Sadeghi, M.; Jervis, R. PoreSpy: A python toolkit for quantitative analysis of porous media images. *J. Open Source Softw.* **2019**, *4*, 1296. https://doi.org/10.21105/joss.01296.
41. Vijayavenkataraman, S.; Zhang, L.; Zhang, S.; Hsi Fuh, J.Y.; Lu, W.F. Triply Periodic Minimal Surfaces Sheet Scaffolds for Tissue Engineering Applications: An Optimization Approach toward Biomimetic Scaffold Design. *ACS Appl. Bio Mater.* **2018**, *1*, 259–269. https://doi.org/10.1021/acsabm.8b00052.
42. Reznikov, N.; Boughton, O.R.; Ghouse, S.; Weston, A.E.; Collinson, L.; Blunn, G.W.; Jeffers, J.R.; Cobb, J.P.; Stevens, M.M. Individual response variations in scaffold-guided bone regeneration are determined by independent strain- and injury-induced mechanisms. *Biomaterials* **2019**, *194*, 183–194. https://doi.org/10.1016/j.biomaterials.2018.11.026.
43. Cipitria, A.; Lange, C.; Schell, H.; Wagermaier, W.; Reichert, J.C.; Hutmacher, D.W.; Fratzl, P.; Duda, G.N. Porous scaffold architecture guides tissue formation. *J. Bone Miner. Res.* **2012**, *27*, 1275–1288. https://doi.org/10.1002/jbmr.1589.
44. Blázquez-Carmona, P.; Mora-Macías, J.; Pajares, A.; Mármol, A.; Reina-Romo, E. On the influence of structural and chemical properties on the elastic modulus of woven bone under healing. *Front. Bioeng. Biotechnol.* **2024**, *12*, 1476473. https://doi.org/10.3389/fbioe.2024.1476473.